




Cite this: *Nanoscale Adv.*, 2019, 1, 799

# Synthesis of nanoporous Mo:BiVO<sub>4</sub> thin film photoanodes using the ultrasonic spray technique for visible-light water splitting†

Sawanta S. Mali,  Gwang Ryeol Park, Hyungjin Kim, Hyun Hoon Kim, Jyoti V. Patil and Chang Kook Hong \*

The use of bismuth vanadate (BiVO<sub>4</sub>) scheelite structures for converting solar energy into fuels and chemicals for fast growth in lab to industrial scale for large-area modules is a key challenge for further development. Herein, we demonstrate a new ultrasonic spray technique as a scalable and versatile coating technique for coating pristine and doped nanoporous BiVO<sub>4</sub> thin film photoanodes directly on FTO-coated glass substrates for water splitting under visible irradiation. The successful Mo doping in BiVO<sub>4</sub> lattice was confirmed by various characterization techniques such as XRD, Raman, EDS and XPS. The Mo:BiVO<sub>4</sub> photoelectrode showed excellent performance with higher stability as compared to pristine BiVO<sub>4</sub> samples.

Received 12th September 2018  
Accepted 7th November 2018

DOI: 10.1039/c8na00209f

rsc.li/nanoscale-advances

## 1. Introduction

Splitting water into hydrogen and oxygen through photoelectrochemical (PEC) solar energy conversion is one of the best approaches for solar fuel applications.<sup>1–4</sup> The complete photoelectrochemical water splitting process includes two half reactions, namely, water reduction and oxidation. However, due to the multistep proton-coupled electron transfer process, water oxidation is more challenging in terms of thermodynamics and kinetics. This process can determine the water splitting efficiency. To date, numerous metal oxides, such as TiO<sub>2</sub>,<sup>5</sup>  $\alpha$ -Fe<sub>2</sub>O<sub>3</sub>,<sup>6</sup> WO<sub>3</sub> (ref. 7) and BiVO<sub>4</sub>,<sup>8–10</sup> have been used as photoanodes for enhancing the oxygen evolution reaction (OER) from water oxidation. From the above-mentioned photoelectrode materials, BiVO<sub>4</sub> is one of the most promising scheelite-type photoanode materials with an appropriate valence band position for OER. So far, BiVO<sub>4</sub> thin films have been deposited by chemical as well as physical techniques such as spin-coating,<sup>11</sup> dip-coating,<sup>12</sup> electrostatic spray/ultrasonic spray pyrolysis,<sup>13–15</sup> reactive magnetron co-sputtering<sup>16</sup> and facile successive ionic layer adsorption and reaction (SILAR).<sup>17</sup> On the other hand, the physical technique of ultrasonic spraying is the most popular and promising technique because of its simplicity, large area production capability and absence of a non-vacuum process.

So far, the ultrasonic spray technique has been used for the synthesis of various nanomaterials including perovskite solar

cells (PSCs). To find commercial applications for solar fuels, it is highly important to develop large-area deposition techniques to fabricate uniform photoelectrodes. Furthermore, it is well-known that nanoarchitectures provide unique properties to improve the performance. Therefore, the synthesis of a uniform nanoporous layer of BiVO<sub>4</sub> is a key parameter in water splitting. Moreover, improving the short diffusion length of BiVO<sub>4</sub> by appropriate dopants, heterojunction formation or metal ion treatment is also important.<sup>18,19</sup> Therefore, an effective deposition technique with positive dopants can help develop onsite applications of solar fuel. Cost saving by using less materials, low maintenance cost, highly uniform deposition for large-area application and simple assembly of equipment are the four main features of the ultrasonic spray technique. Herein, we report the synthesis of nanoporous BiVO<sub>4</sub> thin films by using the ultrasonic spray technique. However, it is well-known that the photoelectrochemical performance of pristine BiVO<sub>4</sub> is limited due to its short carrier diffusion length, which restricts the thickness of the photoelectrodes.<sup>20</sup> Therefore, the synthesized nanoporous BiVO<sub>4</sub> photoelectrodes have been used for water splitting under visible-light irradiation.

## 2. Experimental details

### 2.1 Chemicals and materials

FTO-coated glass substrates were purchased from TEC15, Pilkington with sheet resistance of  $\sim 8 \Omega \text{ cm}^{-1}$ . Precursors such as Bi(NO<sub>3</sub>)<sub>3</sub>·5H<sub>2</sub>O, NH<sub>4</sub>VO<sub>3</sub>, (NH<sub>4</sub>)MoO<sub>4</sub> and HNO<sub>3</sub> were purchased from Sigma Aldrich. Double distilled water was used for the preparation of precursor solutions. All these chemicals were used without further purification.

Polymer Energy Materials Laboratory, School of Applied Chemical Engineering, Chonnam National University, Gwangju, 61186, South Korea. E-mail: sawantasolar@gmail.com; hongck@chonnam.ac.kr

† Electronic supplementary information (ESI) available. See DOI: 10.1039/c8na00209f



## 2.2 Preparation of BiVO<sub>4</sub> thin film electrodes

The FTO-coated glass substrates were cleaned with detergent, water and ethanol. A feeding solution containing 0.2–3 mmol of Bi(NO<sub>3</sub>)<sub>3</sub>·5H<sub>2</sub>O (Sigma Aldrich; 99.9%) and NH<sub>4</sub>VO<sub>3</sub> (Sigma Aldrich; 99.9%) in an equal molar ratio was dissolved in 10 mL of aqueous nitric acid (HNO<sub>3</sub>) solution (2 mol L<sup>−1</sup>) to form a transparent yellow precursor solution. To incorporate Mo doping, we prepared 50 mM ammonium molybdate ((NH<sub>4</sub>)<sub>2</sub>MoO<sub>4</sub>) stock solution. The desired amount of Mo stock solution was added to the above precursor to obtain Mo:BiVO<sub>4</sub> sample. We selected 3% Mo-doping according to previous reports.<sup>20</sup> Spray coating was performed with an ultrasonic spray system (SonoZap, Ultrasonic Atomizer Corp.). The ultrasonic nozzle (Model: WS130K50S304, Wide Spray Atomizer Nozzle) was fixed to a 130 kHz digital ultrasonic generator and the feeding rate was controlled by a syringe pump (KD Scientific). The nozzle to substrate distance was 10 cm and the precursor solution was sprayed at the rate of 0.5 mL h<sup>−1</sup> on the FTO substrate kept at 150 °C on a hot plate in an open atmosphere, as shown in Fig. 1. The prepared light yellow films were further annealed at 450 °C for 1 h and used for further characterizations.

## 2.3 Characterizations

The top-surface and cross-sectional images of un-doped and Mo-doped BiVO<sub>4</sub> thin films were recorded by a scanning electron microscope (SEM; S-4700, Hitachi). Transmission electron microscopy (TEM) micrographs, selected area electron diffraction (SAED) patterns and high-resolution transmission electron microscopy (HRTEM) images were obtained by TECNAI F20 Philips operated at 200 kV. X-ray diffraction (XRD)

measurements were carried out using a D/MAX Ultima III XRD diffractometer (Rigaku, Japan) with Cu-Kα line at 1.5410 Å. The elemental analysis of the deposited samples was performed using an X-ray photoelectron spectrometer (XPS) (VG Multilab 2000-Thermo Scientific, USA, K-Alpha) with a multi-channel detector, which can endure high photonic energies from 0.1 to 3 keV. The micro-Raman spectra of the BiVO<sub>4</sub> samples were recorded in the spectral range of 100–1000 cm<sup>−1</sup> using a micro-Raman spectrometer (JASCO, NRS-5100 Raman microscope) that employed a He-Ne laser source with an excitation wavelength of 633 nm and resolution of 1 cm<sup>−1</sup> at 15 mW laser power.

## 2.4 Photoelectrochemical measurements

The photoelectrochemical (PEC) properties of un-doped and Mo-doped BiVO<sub>4</sub> photoanodes were evaluated using Iviumstat (Ivium Technologies B.V., Eindhoven, the Netherlands) with a three-electrode H-type cell divided into working and counter electrode compartments by Nafion 117 (DuPont) (Fig. 6). Pristine or Mo-doped BiVO<sub>4</sub> thin film electrode, a Pt electrode, and a saturated Ag/AgCl electrode were used as the working, counter, and reference electrodes, respectively. Also, 0.5 mol L<sup>−1</sup> of aqueous Na<sub>2</sub>SO<sub>4</sub> solution in potassium buffer solution (K-Pi, pH 7) was used as the electrolyte. An aqueous phosphate buffer solution [0.1 mol L<sup>−1</sup> KH<sub>2</sub>PO<sub>3</sub> (Sigma Aldrich; 99.6%), 0.1 mol L<sup>−1</sup> K<sub>2</sub>HPO<sub>4</sub> (Sigma Aldrich; 99.5%)] was employed to adjust the pH to 7 [ $E_{(\text{RHE})} = E_{(\text{Ag/AgCl})} + 0.1976 \text{ V} + 0.0591 \text{ pH}$ ]. Nitrogen was initially purged through the solution to remove trace oxygen. Simulated solar illumination was obtained by passing light from a 300 W Xe arc lamp through an AM 1.5 G filter. The power density of the incident light was

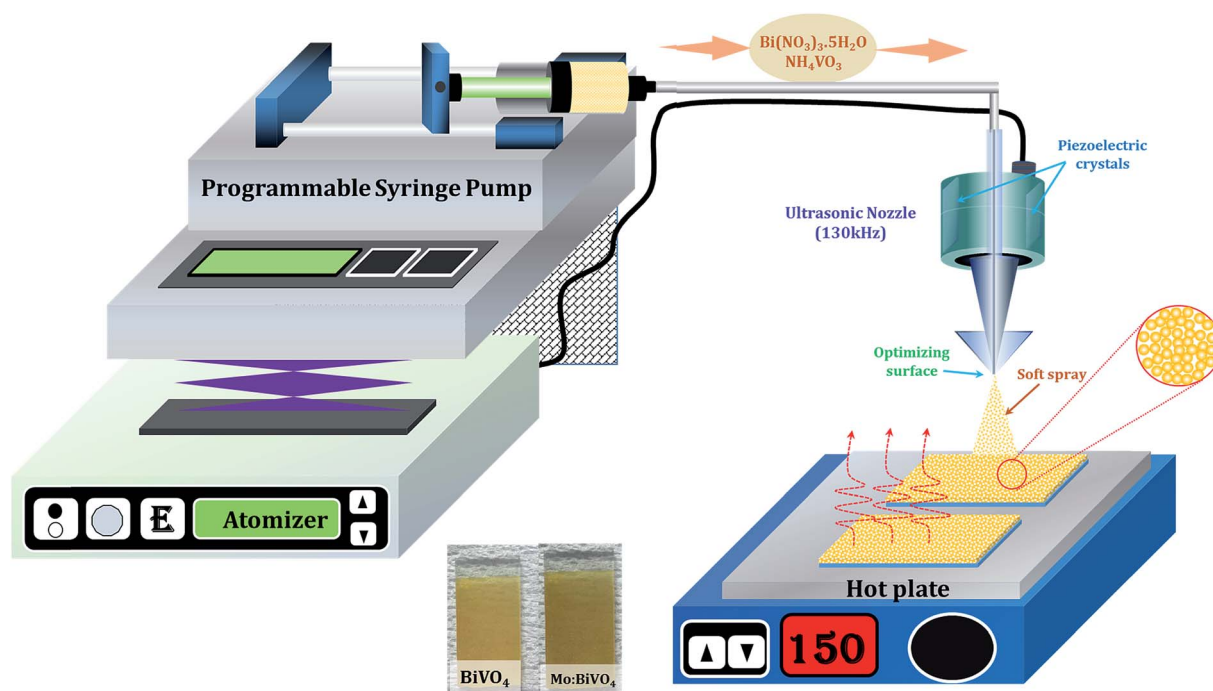


Fig. 1 Schematic of concurrently pumped ultrasonic spray coating for pristine and Mo-doped BiVO<sub>4</sub> thin film deposition.



calibrated to  $100 \text{ mW cm}^{-2}$  by using a thermopile detector and a National Renewable Energy Laboratory – certified reference cell.  $J$ - $V$  curves were measured by sweeping the potential in the positive direction at a scan rate of  $10 \text{ mV s}^{-1}$  in dark and under illumination. Electrochemical impedance spectroscopy (EIS) was conducted using Iviumstat (Ivium Technologies B.V., Eindhoven, the Netherlands) at an open-circuit potential at frequencies ranging from  $10^{-1}$  to  $10^5 \text{ Hz}$  with AC amplitude of  $10 \text{ mV}$ .

### 3. Results and discussion

The surface morphology of the as-deposited samples was studied by scanning electron microscopy (SEM) (Fig. S1†). The SEM micrograph of as-deposited pristine  $\text{BiVO}_4$  sample exhibited irregular deposition and agglomeration of nanoparticles (Fig. S1a†), whereas as-deposited  $\text{Mo:BiVO}_4$  showed uniform coating with porous nanostructures (Fig. S1b†). To crystallize and remove the remaining solvent, we annealed these samples at  $450^\circ\text{C}$  for 2 h. Fig. 2 shows the top view and cross sectional SEM images of pristine and  $\text{Mo:BiVO}_4$  thin films at different magnifications. The pristine  $\text{BiVO}_4$  sample showed agglomerated nanoparticle morphology. In contrast, the  $\text{Mo:BiVO}_4$  sample showed more nanoporous networks compared to pristine sample. These networks along with porous nanostructures were obtained due to volatilization of  $\text{H}_2\text{O}$  and  $\text{HNO}_3$  and decomposition of by-products. To check the thickness of fabricated  $\text{Mo:BiVO}_4$  photoelectrode, scanning electron microscopy (SEM) images were acquired for both samples. The SEM micrographs revealed that the surface of FTO substrate was uniformly coated with  $\text{BiVO}_4$  films with  $1.1\text{--}1.2 \mu\text{m}$  thickness. This nanoporous architecture facilitated better penetration of aqueous  $\text{Na}_2\text{SO}_4$  electrolyte solution into either  $\text{BiVO}_4$  or  $\text{Mo:BiVO}_4$  films.

Fig. 3 shows the XRD patterns of un-doped  $\text{BiVO}_4$  and  $\text{Mo:BiVO}_4$  thin film samples. The XRD patterns revealed the formation of single phase  $\text{BiVO}_4$  crystals with scheelite

structures and monoclinic phase.<sup>21</sup> The lattice constants were calculated to be  $a = 5.0195 \text{ \AA}$ ,  $b = 11.701 \text{ \AA}$ , and  $c = 5.092 \text{ \AA}$ , which matched well with literature data (JCPDS no. 014-0688). On the other hand,  $\text{Mo-doped BiVO}_4$  did not show any significant peak for Mo doping, which might be due to weak diffraction intensities of Mo compared to those of pristine  $\text{BiVO}_4$  or due to very less amount of Mo (2%) employed in this synthesis. However, the characteristic peak of  $\text{Mo:BiVO}_4$  sample at  $2\theta = 28.822^\circ$  corresponding to the  $(hkl)$  plane  $(-121)$  slightly shifted and appeared at  $2\theta = 28.889^\circ$  due to compressive lattice strain.<sup>22</sup> Furthermore, the peak for  $(-130)$  at  $2\theta = 28.586^\circ$  disappeared. Raman spectra showed the same features for pristine  $\text{BiVO}_4$  and  $\text{Mo:BiVO}_4$  thin films (Fig. 4). The prominent peak at  $827.53 \text{ cm}^{-1}$  was assigned to stretching mode  $\nu_s$  ( $\text{V-O}$ ) vibration.

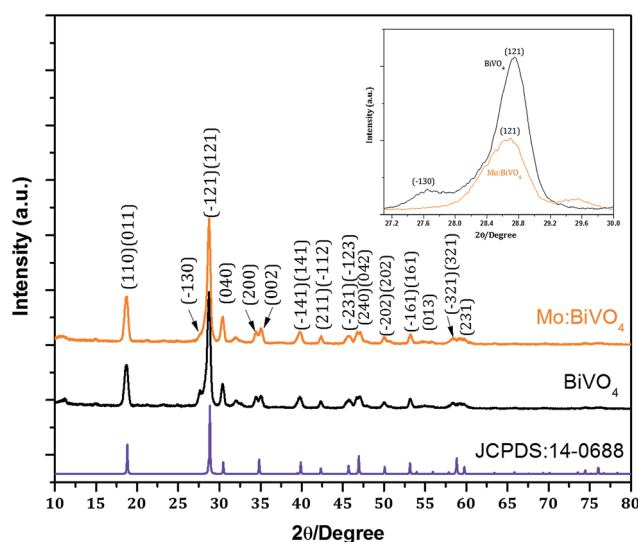


Fig. 3 XRD patterns of bare  $\text{BiVO}_4$  and  $\text{Mo:BiVO}_4$  thin films synthesized by the ultrasonic spray technique. For comparison, standard diffraction pattern of JCPDS no. 14-0688 is given. The inset shows characteristic peak shift to higher angle  $2\theta$  position.

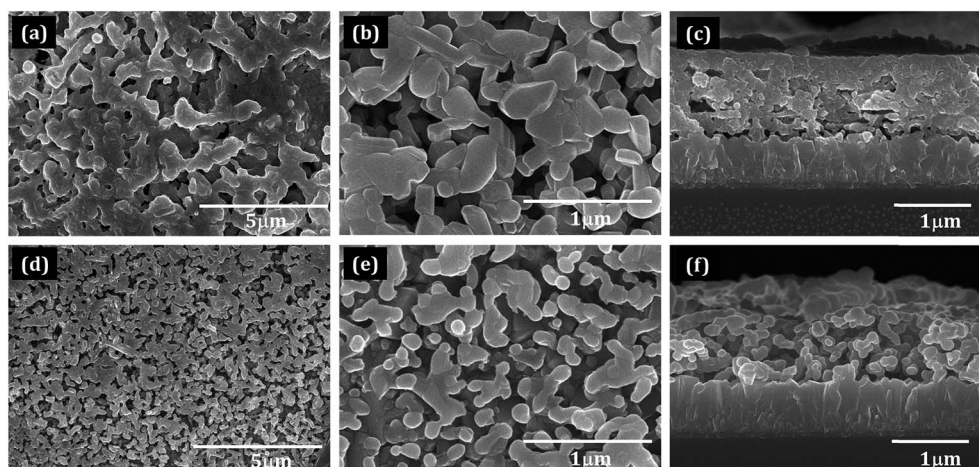


Fig. 2 Scanning electron microscopy images of pristine  $\text{BiVO}_4$  (a and b) and  $\text{Mo:BiVO}_4$  (d and e) thin films deposited by the ultrasonic technique. (c) Cross-section of  $\text{BiVO}_4$  thin film electrodes. (f) Cross-section of  $\text{Mo:BiVO}_4$  thin film electrodes (both samples were annealed at  $450^\circ\text{C}$  for 2 h).





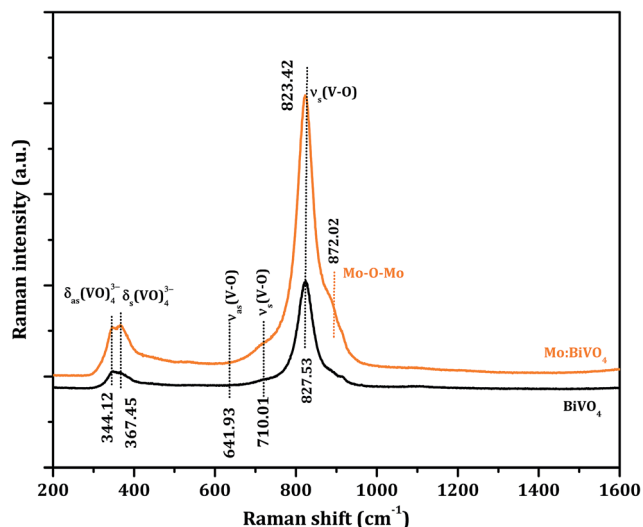


Fig. 4 Raman spectra of  $\text{BiVO}_4$  and  $\text{Mo:BiVO}_4$  nanoporous thin films.

Careful observation revealed a weak shoulder at  $710\text{ cm}^{-1}$  corresponding to  $\nu_{\text{as}}(\text{V-O})$ . The  $\delta_{\text{as}}(\text{VO})_4^{3-}$  and  $\delta_{\text{s}}(\text{VO})_4^{3-}$  modes were around  $344.12$  and  $367.45\text{ cm}^{-1}$ . For  $\text{Mo:BiVO}_4$ , the V-O stretching mode shifted to a lower wavenumber ( $823.42\text{ cm}^{-1}$ ) as compared to  $827.53\text{ cm}^{-1}$  for  $\text{BiVO}_4$ , which revealed that the short-range symmetry of  $\text{VO}_4$  tetrahedron increased. This Raman shift indicated that longer V-O bond length was observed because V was replaced with Mo in  $\text{VO}_4$  tetrahedron.<sup>23–25</sup> The Raman spectrum also showed a satellite peak at  $872.02\text{ cm}^{-1}$  corresponding to the Mo-O-Mo stretching mode.

For in-depth analysis, we have recorded TEM/HRTEM of  $\text{Mo:BiVO}_4$  sample. Fig. 5 shows the TEM images of  $\text{Mo:BiVO}_4$  sample at different magnifications. The HRTEM images and SAED pattern were recorded to analyse the crystal structures of the  $\text{Mo:BiVO}_4$  nanoporous sample. The SAED intense ring pattern (Fig. 5b inset) revealed that synthesized  $\text{Mo:BiVO}_4$  is highly crystalline in nature. The HRTEM analysis of  $\text{Mo:BiVO}_4$  was confirmed from the continuous bright long lattice fringes with interplanar lattice spacing of  $d_{130} = 0.312\text{ nm}$  between the

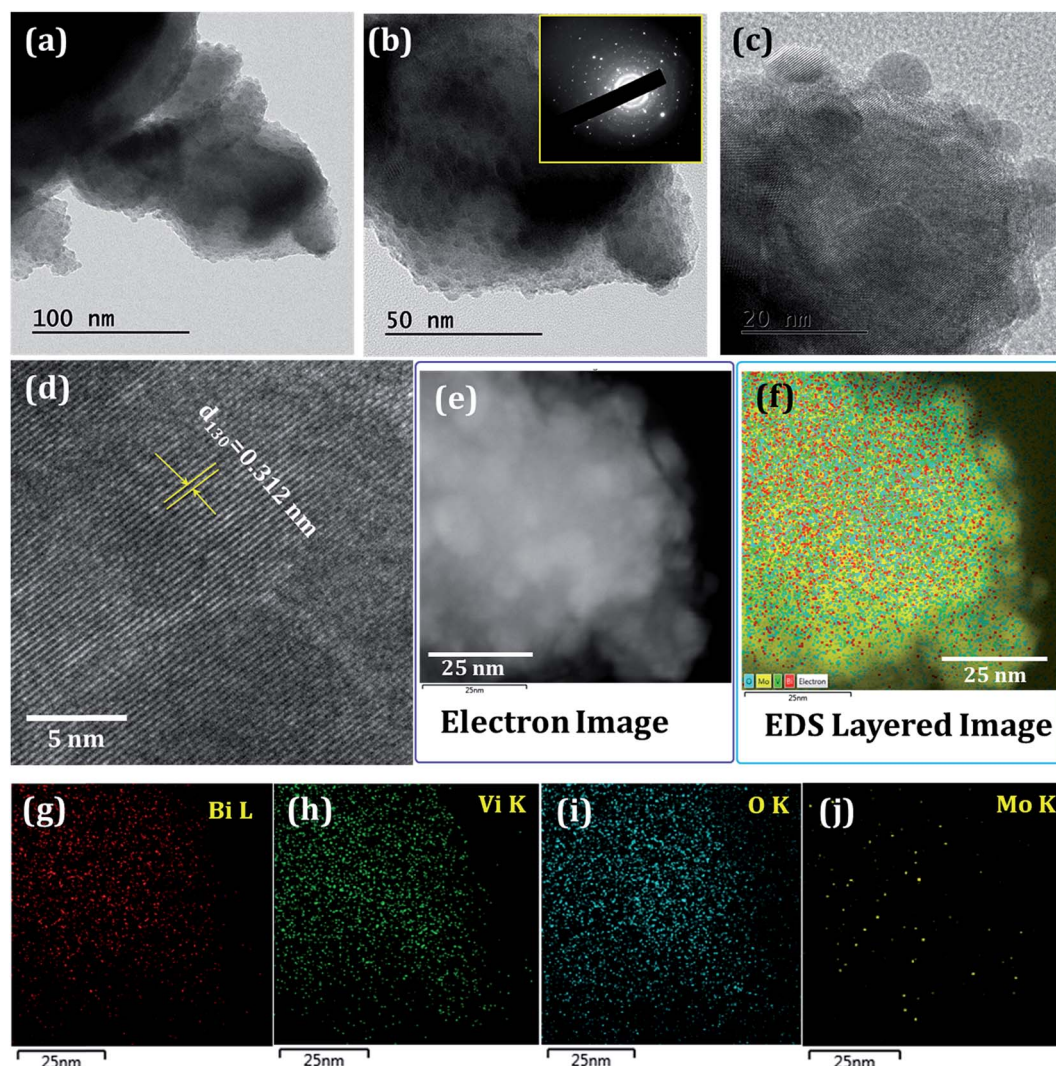


Fig. 5 (a–c) TEM images of  $\text{Mo:BiVO}_4$  sample at different magnifications (the inset in b shows the SAED pattern); (d) HRTEM image; (e–j) the corresponding STEM and EDS element mapping images for Bi, V, O and Mo.



adjacent lattice fringes, as shown in Fig. 5d. The highly polycrystalline nature of  $\text{BiVO}_4$  was confirmed from the continuous bright long lattice fringes. The elemental analysis was confirmed by recording STEM/EDS elemental mapping (Fig. 5e–j). The elemental mapping confirmed the uniform distribution of bismuth, vanadium, oxygen and molybdenum throughout the surface. The calculated Mo doping percentage was  $\sim 1.85\%$ .<sup>26,27</sup> Optical properties of these samples were confirmed by UV-Vis spectroscopy, as shown in Fig. S2.† Both electrodes showed typical light absorption in the UV and visible wavelength ranges. The band edge for  $\text{BiVO}_4$  thin film sample was observed at nearly 515 nm, which further increased up to 537 nm. From the Tauc plots, it was observed that the initial band-gap of 2.41 eV reduced to 2.31 eV due to Mo doping.

Chemical compositions of un-doped and  $\text{Mo:BiVO}_4$  samples were analysed by XPS (Fig. 6). The binding energies of pristine  $\text{BiVO}_4$  sample for  $\text{Bi}(4f_{5/2})$  and  $\text{Bi}(4f_{7/2})$  core levels were located at 163.77 and 158.47 eV, respectively; however, for the  $\text{Mo:BiVO}_4$  sample, these core levels slightly shifted toward higher energy and appeared at 163.96 and 158.59 eV, respectively. Besides, the binding energies of V 2p showed negligible difference between  $\text{BiVO}_4$  and  $\text{Mo:BiVO}_4$  (Fig. 6a). In contrast, the V 2p states at 523.70 and 516.45 eV for  $\text{BiVO}_4$  slightly shifted to 524.36 and 516.82 eV for  $\text{Mo:BiVO}_4$  (Fig. 6b). This shift may be caused by different electronegativities of  $\text{Mo}^{6+}$  and  $\text{V}^{5+}$ . The two peaks at 529.5 and 531.3 eV were ascribed to the lattice oxygen (O 1s) of  $\text{BiVO}_4$  crystal and –OH groups formed on the surface of both

samples, respectively (Fig. 6c). The above results support the conclusion that  $\text{Mo}^{6+}$  ions can be substituted for  $\text{Bi}^{3+}$  ions in  $\text{BiVO}_4$ .<sup>28,29</sup> The binding energy of  $\text{Mo}(3d_{5/2})$  at 231.47 eV and  $\text{Mo}(3d_{3/2})$  at 234.7 eV showed that Mo is present in 6+ oxidation state (Fig. 6d).<sup>22,30</sup> No additional phases were observed. Furthermore, the doping concentration of  $\text{Mo:BiVO}_4$  was determined to be  $\sim 2\%$  via XPS spectra. These results are also consistent with the results of EDS (Fig. S3†) and XPS analyses (Fig. S4†).

The photoelectrochemical properties of undoped and Mo doped  $\text{BiVO}_4$  thin films were tested in an H-cell two-compartment cell composed of FTO/ $\text{BiVO}_4$  as the photoanode, Ag/AgCl as the reference electrode and Pt mesh as the counter electrode. The experimental arrangement for photocurrent measurements is shown in Fig. 7a. Here, Nafion 117 membrane was used to separate the cathode and anode compartments. A three-electrode cell configuration was used for the measurements. FTO/ $\text{BiVO}_4$ , Ag/AgCl and Pt mesh were used as the working electrode, reference electrode and counter electrode, respectively. Fig. 7b shows the processes in which the holes react with  $\text{OH}^-$  in the electrolyte to produce oxygen ( $4\text{OH}^- + 4\text{h}^+ \rightarrow 2\text{H}_2\text{O} + \text{O}_2$ ).<sup>16</sup> At the same time, the electrons can transfer to the counter electrode (Pt electrode) to react with water to produce hydrogen ( $2\text{H}_2\text{O} + 2\text{e}^- \rightarrow \text{H}_2 + 2\text{OH}^-$ ). This results in a photocurrent, and its intensity mainly depends on the charge carrier separation rate and thus can reflect true water splitting. The photocurrent generation activity of both type of samples was studied under  $100 \text{ mW cm}^{-2}$  (AM 1.5 G) illumination in

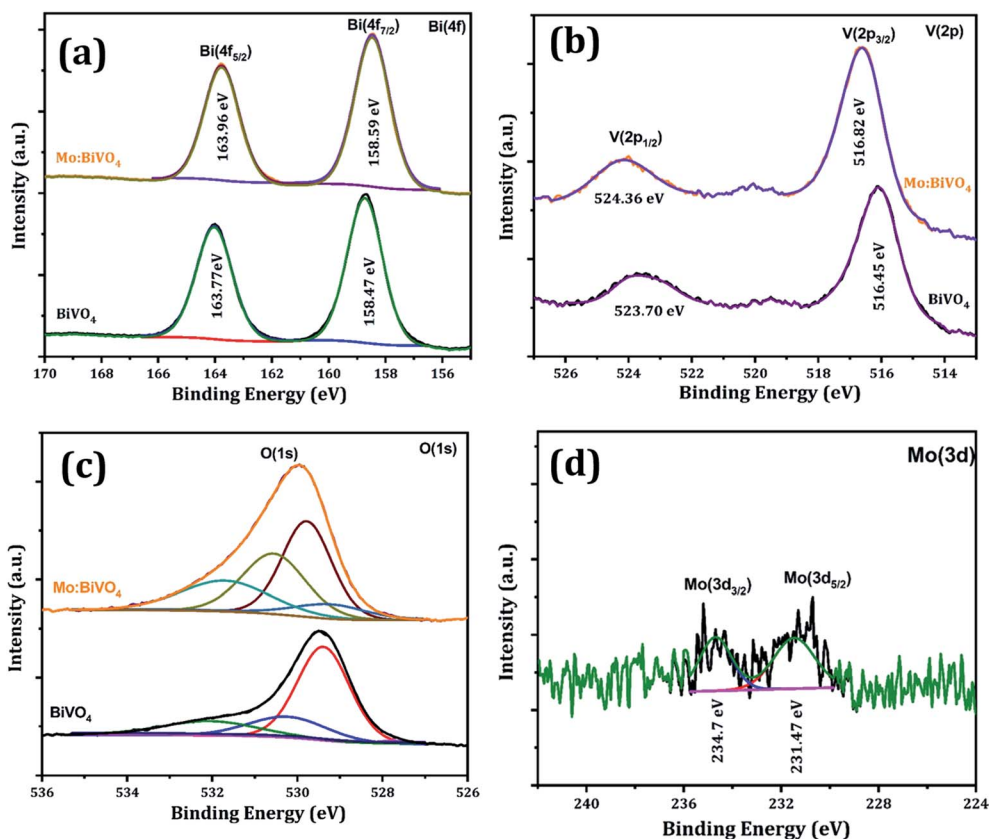


Fig. 6 XPS spectra of pristine  $\text{BiVO}_4$  and  $\text{Mo:BiVO}_4$  thin films; high-resolution core level XPS spectrum of (a) Bi 4f (b), V 2p (c), O 1s (d) and Mo 3d.



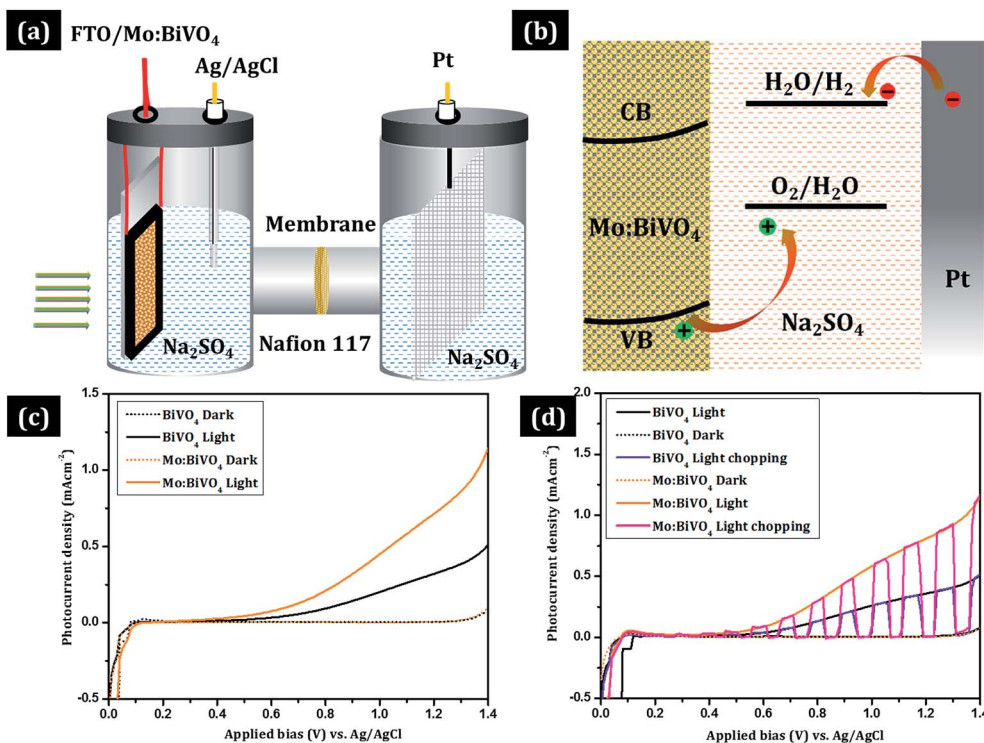


Fig. 7 (a) Experimental set-up of an H-shaped photoelectrochemical cell with two separate compartments for photocatalytic oxidation of water to  $O_2$ ; (b) mechanism of photoelectrochemical water splitting; (c) photocurrent density–potential curves recorded under dark (dotted line) and light (solid line) (scan rate =  $10 \text{ mV s}^{-1}$ ); (d) chopping performance.

0.5 M  $Na_2SO_4$  electrolyte. The measured photocurrent–density curves *versus* applied potential for both type of electrodes are shown in Fig. 7c. During measurement of current in the dark, a very negligible current of  $\sim 0.05 \text{ mA cm}^{-2}$  was observed at  $\sim 1.3 \text{ V}$  (*vs.* Ag/AgCl), which may be due to the non-faradic reaction. To measure the rate of hydrogen and oxygen production by water splitting, current–voltage measurements are the best option. Fig. 7c shows the  $J$ – $V$  plots of pristine  $BiVO_4$  and Mo:BiVO<sub>4</sub> samples measured under illumination. It is clear that the photo-generated current density for Mo:BiVO<sub>4</sub> is much higher than that of pristine  $BiVO_4$ . This enhanced photoelectrochemical water oxidation for Mo:BiVO<sub>4</sub> can be ascribed to the enhanced hole diffusion length and increased charge separation, which reduces the charge transfer resistance for water oxidation. Furthermore, it is noted that Mo doping facilitates improved electron mobility. It is also noted that the nanoporous network facilitates enhanced electronic transport due to Mo doping. Interestingly, these photoelectrodes are quite stable and show good photocurrent stability as well as switching behaviour (Fig. 7d).<sup>30</sup> Electrochemical impedance spectroscopy (EIS) measurements of pristine sample and Mo:BiVO<sub>4</sub> sample were further obtained to investigate the charge transfer resistance and separation efficiency. As shown in Fig. 8, the arc radius of Mo:BiVO<sub>4</sub> under light is smaller than that of pristine  $BiVO_4$ , thus indicating that Mo:BiVO<sub>4</sub> has lower resistance than pristine  $BiVO_4$  and accelerated interfacial charge-transfer process. To check the long-term stability under chopped light, we recorded the transient properties of  $BiVO_4$  (Fig. S5a and

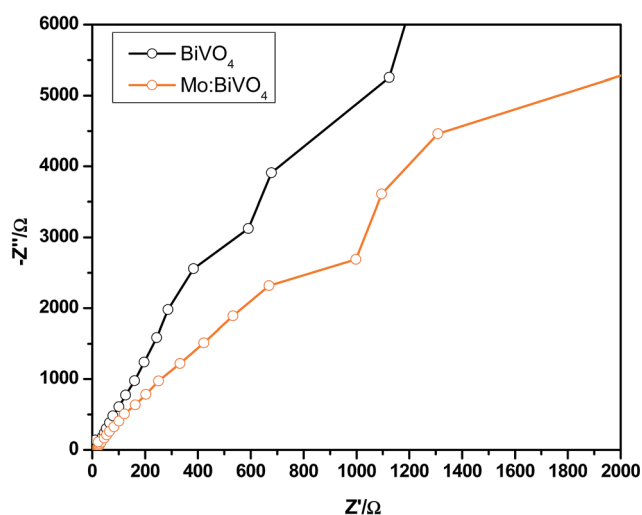


Fig. 8 Electrochemical impedance spectroscopy (EIS) of pristine and Mo:BiVO<sub>4</sub> samples under illumination.

S5b†) and Mo:BiVO<sub>4</sub> (Fig. S5c and S5d†) electrodes in  $Na_2SO_4$  electrolyte (Fig. S5†). The pristine  $BiVO_4$  sample initially shows  $0.241 \text{ mA cm}^{-2}$  current density, which further decreases up to  $0.185 \text{ mA cm}^{-2}$  after 500 s; furthermore, decrease is observed up to  $0.140 \text{ mA cm}^{-2}$  after 3600 s. However, in the case of Mo:BiVO<sub>4</sub>, the initial current density of  $0.618 \text{ mA cm}^{-2}$  decreases slightly up to  $0.594 \text{ mA cm}^{-2}$  at 200 s, and there is no observable decrease up to 3600 s. From stability analysis, it is





clear that the Mo:BiVO<sub>4</sub> sample shows much higher stability and performance than the pristine BiVO<sub>4</sub> electrode.

## 4. Conclusions

In conclusion, we have successfully developed a new method to synthesize pristine and doped BiVO<sub>4</sub> nanoporous thin films using the ultrasonic spray technique for efficient water splitting under visible-light irradiation. The pristine and Mo-doped BiVO<sub>4</sub> nanoporous thin films were characterized by XRD, HRTEM and XPS. Our water splitting results revealed enhanced photocurrent density for Mo:BiVO<sub>4</sub> against that for pristine BiVO<sub>4</sub> due to the nanoporous structure and Mo doping. The present ultrasonic spray technique opens a new approach toward large-area deposition of nanoporous BiVO<sub>4</sub> photoelectrodes for onsite applications.

## Conflicts of interest

There are no conflicts to declare.

## Acknowledgements

This research was supported by the National Research Foundation of Korea (NRF) (NRF-2017R1A2B4008117). This work was also supported by the Korea Research Fellowship Program through the National Research Foundation of Korea (NRF) funded by the Ministry of Science, ICT and Future Planning (2016H1D3A1909289) for an outstanding overseas young researcher. This work was supported by Priority Research Centers Program through the National Research Foundation of Korea (NRF) funded by the Ministry of Education, Science and Technology (2018R1A6A1A03024334).

## References

- 1 A. Fujishima and K. Honda *Electrochemical Photolysis of Water at a Semiconductor Electrode Nature*, 1972, vol. 238, pp. 37–38.
- 2 K. Ohashi, J. Mccann and J. O. Bockris, Stable Photoelectrochemical Cells for Splitting of Water, *Nature*, 1977, **266**, 610–611.
- 3 M. G. Walter, E. L. Warren, J. R. McKone, S. W. Boettcher, Q. Mi, E. A. Santori and N. S. Lewis, Solar Water Splitting Cells, *Chem. Rev.*, 2010, **110**, 6446–6473.
- 4 T. Hisatomi, J. Kubota and K. Domen, Recent Advances in Semiconductors for Photocatalytic and Photoelectrochemical Water Splitting, *Chem. Soc. Rev.*, 2014, **43**, 7520–7535.
- 5 L. Li, L. Yu, Z. Lin and G. Yang, Reduced TiO<sub>2</sub>-Graphene Oxide Heterostructure as Broad Spectrum-Driven Efficient Water-Splitting Photocatalysts, *ACS Appl. Mater. Interfaces*, 2016, **8**, 8536–8545.
- 6 H. Dotan, K. Sivula, M. Gratzel, A. Rothschild and S. C. Warren, Probing the Photoelectrochemical Properties of Hematite ( $\alpha$ -Fe<sub>2</sub>O<sub>3</sub>) Electrodes Using Hydrogen Peroxide as a Hole Scavenger, *Energy Environ. Sci.*, 2011, **4**, 958–964.
- 7 P. Dias, T. Lopes, L. Meda, L. Andradea and A. Mendes, Photoelectrochemical Water Splitting Using WO<sub>3</sub> Photoanodes: The Substrate and Temperature Roles, *Phys. Chem. Chem. Phys.*, 2016, **18**, 5232–5243.
- 8 R. Li, F. Zhang, D. Wang, J. Yang, M. Li, J. Zhu, X. Zhou, H. Han and C. Li, Spatial Separation of Photogenerated Electrons and Holes Among {010} and {110} Crystal Facets of BiVO<sub>4</sub>, *Nat. Commun.*, 2013, **4**, 1432.
- 9 L. Chen, F. M. Toma, J. K. Cooper, A. Lyon, Y. Lin, I. D. Sharp and J. W. Ager, Mo-doped BiVO<sub>4</sub> Photoanodes Synthesized by Reactive Sputtering, *ChemSusChem*, 2015, **8**, 1066–1071.
- 10 S. K. Pilli, T. E. Furtak, L. D. Brown, T. G. Deutsch, J. A. Turner and A. M. Herring, Cobaltphosphate (Co-Pi) Catalyst Modified Mo-doped BiVO<sub>4</sub> Photoelectrodes for Solar Water Oxidation, *Energy Environ. Sci.*, 2011, **4**, 5028–5034.
- 11 Q. Jia, K. Iwashina and A. Kudo, Facile Fabrication of an Efficient BiVO<sub>4</sub> Thin Film Electrode for Water Splitting Under Visible Light Irradiation, *Proc. Natl. Acad. Sci. U. S. A.*, 2012, **109**, 11564–11569.
- 12 S. Hilliard, D. Friedrich, S. Kressman, H. Strub, V. Artero and C. Laberty-Rober, Solar-Water-Splitting BiVO<sub>4</sub> Thin-Film Photoanodes Prepared By Using a Sol-Gel Dip-Coating Technique, *ChemPhotoChem*, 2017, **1**, 273–280.
- 13 X. Liu, Y. Liu, J. Su, M. Li and L. Guo, Facile Preparation of BiVO<sub>4</sub> Nanoparticle Film by Electrostatic Spray Pyrolysis for Photoelectrochemical Water Splitting, *Int. J. Hydrogen Energy*, 2015, **40**, 12964–12972.
- 14 M. Li, Z. Liang and L. Guo, Preparation and Photoelectrochemical Study of BiVO<sub>4</sub> Thin Films Deposited by Ultrasonic Spray Pyrolysis, *Int. J. Hydrogen Energy*, 2010, **35**, 7127–7133.
- 15 S. S. Dunkle, R. J. Helmich and K. S. Suslick, BiVO<sub>4</sub> as a Visible-Light Photocatalyst Prepared by Ultrasonic Spray Pyrolysis, *J. Phys. Chem. C*, 2009, **113**, 11980–11983.
- 16 H. Gong, N. Freudenberg, M. Nie, R. van de Krol and K. Ellmer, BiVO<sub>4</sub> Photoanodes for Water Splitting with High Injection Efficiency, Deposited by Reactive Magnetron Co-sputtering, *AIP Adv.*, 2016, **6**, 045108.
- 17 Y. Li, J. Zhu, H. Chu, J. Wei, F. Liu, M. Lv, J. Tang, B. Zhang, J. Yao, Z. Huo, L. Hu and S. Dai, BiVO<sub>4</sub> semiconductor sensitized solar cells, *Sci. China: Chem.*, 2015, **58**, 148.
- 18 Y. Pihosh, I. Turkevych, K. Mawatari, J. Uemura, Y. Kazoe, S. Kosar, K. Makita, T. Sugaya, T. Matsui, D. Fujita, M. Tosa, M. Kondo and T. Kitamori, Photocatalytic generation of hydrogen by core-shell WO<sub>3</sub>/BiVO<sub>4</sub> nanorods with ultimate water splitting efficiency, *Sci. Rep.*, 2015, **5**, 11141, DOI: 10.1038/srep11141.
- 19 K. Sayama, A. Nomura, T. Arai, T. Sugita, R. Abe, M. Yanagida, T. Oi, Y. Iwasaki, Y. Abe and H. Sugihara, Photoelectrochemical Decomposition of Water into H<sub>2</sub> and O<sub>2</sub> on Porous BiVO<sub>4</sub> Thin-Film Electrodes under Visible Light and Significant Effect of Ag Ion Treatment, *J. Phys. Chem. B*, 2006, **110**(23), 11352–11360.
- 20 Y. Qiu, W. Liu, W. Chen, W. Chen, G. Zhou, P. C. Hsu, R. Zhang, Z. Liang, S. Fan, Y. Zhang and Y. Cui, Efficient



- Solar-Driven Water Splitting by Nanocone BiVO<sub>4</sub>-Perovskite Tandem Cells, *Sci. Adv.*, 2016, **2**, e1501764.
- 21 L. Zhang, D. Chen and X. Jiao, Monoclinic Structured BiVO<sub>4</sub> Nanosheets: Hydrothermal Preparation, Formation Mechanism, and Coloristic and Photocatalytic Properties, *J. Phys. Chem.*, 2006, **110**, 2668–2673.
  - 22 Z. Jiang, Y. Liu, T. Jing, B. Huang, X. Zhang, X. Qin, Y. Dai and M. H. Whangbo, Enhancing the Photocatalytic Activity of BiVO<sub>4</sub> for Oxygen Evolution by Ce Doping: Ce<sup>3+</sup> Ions as Hole Traps, *J. Phys. Chem. C*, 2016, **120**, 2058–2063.
  - 23 V. I. Merupo, S. Velumani, G. Oza, M. Makowska-Janusik and A. Kassiba, Structural, Electronic and Optical Features of Molybdenum-Doped Bismuth Vanadium Oxide, *Mater. Sci. Semicond. Process.*, 2015, **31**, 618–623.
  - 24 M. S. Jang, H. L. Park, J. N. Kim, J. H. Ro and Y. H. Park, Raman Spectrum in Monoclinic BiVO<sub>4</sub>, *Jpn. J. Appl. Phys.*, 1985, **24**, 506–507.
  - 25 R. L. Frost, D. A. Henry, M. L. Weier and W. Martens, Raman Spectroscopy of Three Polymorphs of BiVO<sub>4</sub>: Clinobisvanite, Dreyerite and Pucherite, With Comparisons to (VO<sub>4</sub>)<sup>3-</sup>-Bearing Minerals: Namibite, Pottsite and Schumacherite, *J. Raman Spectrosc.*, 2006, **37**, 722–732.
  - 26 S. M. Thalluri, C. M. Suarez, M. Hussain, S. Hernandez, A. Virga, G. Saracco and N. Russo, Evaluation of the Parameters Affecting the Visible-Light-Induced Photocatalytic Activity of Monoclinic BiVO<sub>4</sub> for Water Oxidation, *Ind. Eng. Chem. Res.*, 2013, **52**, 17414.
  - 27 Q. Wang, J. He, Y. Shi, S. Zhang, T. Niu, H. She and Y. Bi, Designing Non-Noble/Semiconductor Bi/BiVO<sub>4</sub> Photoelectrode for the Enhanced Photoelectrochemical Performance, *Chem. Eng. J.*, 2017, **326**, 411–418.
  - 28 R. P. Antony, P. S. Bassi, F. F. Abdi, S. Y. Chiam, Y. Ren, J. Barber, J. S. C. Loo and L. H. Wong, Electrospun Mo-BiVO<sub>4</sub> for Efficient Photoelectrochemical Water Oxidation: Direct Evidence of Improved Hole Diffusion Length and Charge Separation, *Electrochim. Acta*, 2016, **211**, 173–182.
  - 29 M. Xie, Z. Zhang, W. Han, X. Cheng, X. Li and E. Xie, Efficient Hydrogen Evolution Under Visible Light Irradiation Over BiVO<sub>4</sub> Quantum Dot Decorated Screw-Like SnO<sub>2</sub> Nanostructures, *J. Mater. Chem. A*, 2017, **5**, 10338–10346.
  - 30 W. Yao, H. Iwai and J. Ye, Effects of Molybdenum Substitution on the Photocatalytic Behavior of BiVO<sub>4</sub>, *Dalton Trans.*, 2008, 1426–1430.

